

Geophysical Research Letters

RESEARCH LETTER

10.1029/2020GL087699

Key Points:

- Wind waves attenuate across the Antarctic sea ice with a narrow directional distribution
- Scattering of waves by ice floes plays a negligible role in wave attenuation
- Observed wave attenuation is consistent with ice breakup modulating the dissipation strength

Supporting Information:

- Supporting Information S1

Correspondence to:

F. Ardhuin,
ardhuin@ifremer.fr

Citation:

Ardhuin, F., Otero, M., Merrifield, S., Grouazel, A., & Terril, E. (2020). Ice breakup controls dissipation of wind waves across Southern Ocean sea ice. *Geophysical Research Letters*, *47*, e2020GL087699. <https://doi.org/10.1029/2020GL087699>

Received 2 MAR 2020

Accepted 4 JUN 2020

Accepted article online 9 JUN 2020

Ice Breakup Controls Dissipation of Wind Waves Across Southern Ocean Sea Ice

Fabrice Ardhuin^{1,2} , Mark Otero¹ , Sophia Merrifield¹ , Antoine Grouazel² , and Eric Terril¹ 

¹Scripps Institution of Oceanography, La Jolla, CA, USA, ²Univ. Brest, CNRS, IRD, Ifremer, Laboratoire d'Océanographie Physique et Spatiale (LOPS), IUEM, Brest, France

Abstract Sea ice inhibits the development of wind-generated surface gravity waves which are the dominant factor in upper ocean mixing and air-sea fluxes. In turn, sea ice properties are modified by wave action. Understanding the interaction of ice and waves is important for characterizing both air-sea interactions and sea ice dynamics. Current leading theory attributes wave attenuation primarily to scattering by ice floes. Here we use new in situ wave measurements to show that attenuation is dominated by dissipation with negligible effect by scattering. Time series of wave height in ice exhibit an “on/off” behavior that is consistent with switching between two states of sea ice: a relatively unbroken state associated with strong damping (off), possibly caused by ice flexure, and very weak attenuation (on) across sea ice that has been broken up by wave action.

Plain Language Summary Waves created by wind at the ocean surface are strongly attenuated when they travel across ice-covered regions. Until now, this effect was thought to be the result of reflection of waves off pieces of ice. Using new measurements of wave directions, we show that waves do not come from a broad range of directions, and scattering must be weak. Instead, we find that attenuation is highly variable and related to the size of ice floes. We hypothesize that attenuation may be caused by cyclic deformation of the ice. When the waves are large enough to break the ice up, this deformation stops, and the attenuation is much less. This finding is important for forecasting waves in ice-infested waters as well as predicting seasonal sea ice extent.

1. Introduction

Recent studies have revealed that ocean waves play a significant role in the ice momentum balance (Stopa et al., 2018), ice extent (Kohout et al., 2014), and the rapid thickening of ice when the ocean freezes (Sutherland & Dumont, 2018). Previous wave measurements in ice-covered waters (Doble & Bidlot, 2013; Kohout et al., 2014) have shown that waves in ice attenuate over longer distances when the open water wave height increases, often due to longer corresponding wave periods (Meylan et al., 2014). This result was used to define an ad hoc parameterization of wave attenuation (Kohout et al., 2016) that fails to reproduce the large range of observed attenuations for any given off-ice wave height and wave period (Stopa et al., 2018). This poor performance calls for a detailed physical understanding of ice-wave interaction processes.

Following early works (Wadhams, 1988), the attenuation of waves that propagate under the ice is generally attributed to scattering (Squire, 2020). Scattering is a partial reflection of waves at the boundaries of ice floes, broadening the distribution of wave directions. Other processes dissipate wave energy into heat and narrow the wave direction distribution around the shortest propagation path. Measured wave directions within the ice can thus reveal the importance of scattering. For example, the narrow directional spread of waves with periods 19 to 23 s measured with directional tilt meters in the Arctic showed that scattering could not be a significant source of attenuation for these very long waves (Ardhuin et al., 2016). Here we generalize these observations to more typical wave periods from 10 to 20 s using wave buoy measurements. We evaluate two different dissipation processes: under-ice friction (Stopa et al., 2016) and the anelastic dissipation associated with ice flexure (Cole et al., 1998). The latter process yields large dissipation rates when the ice is flexing. However, flexing only occurs for waves shorter than about twice the ice floe diameter as floes tilt over longer waves (Boutin et al., 2018). This varying behavior as a function of wavelength and floe size can explain the

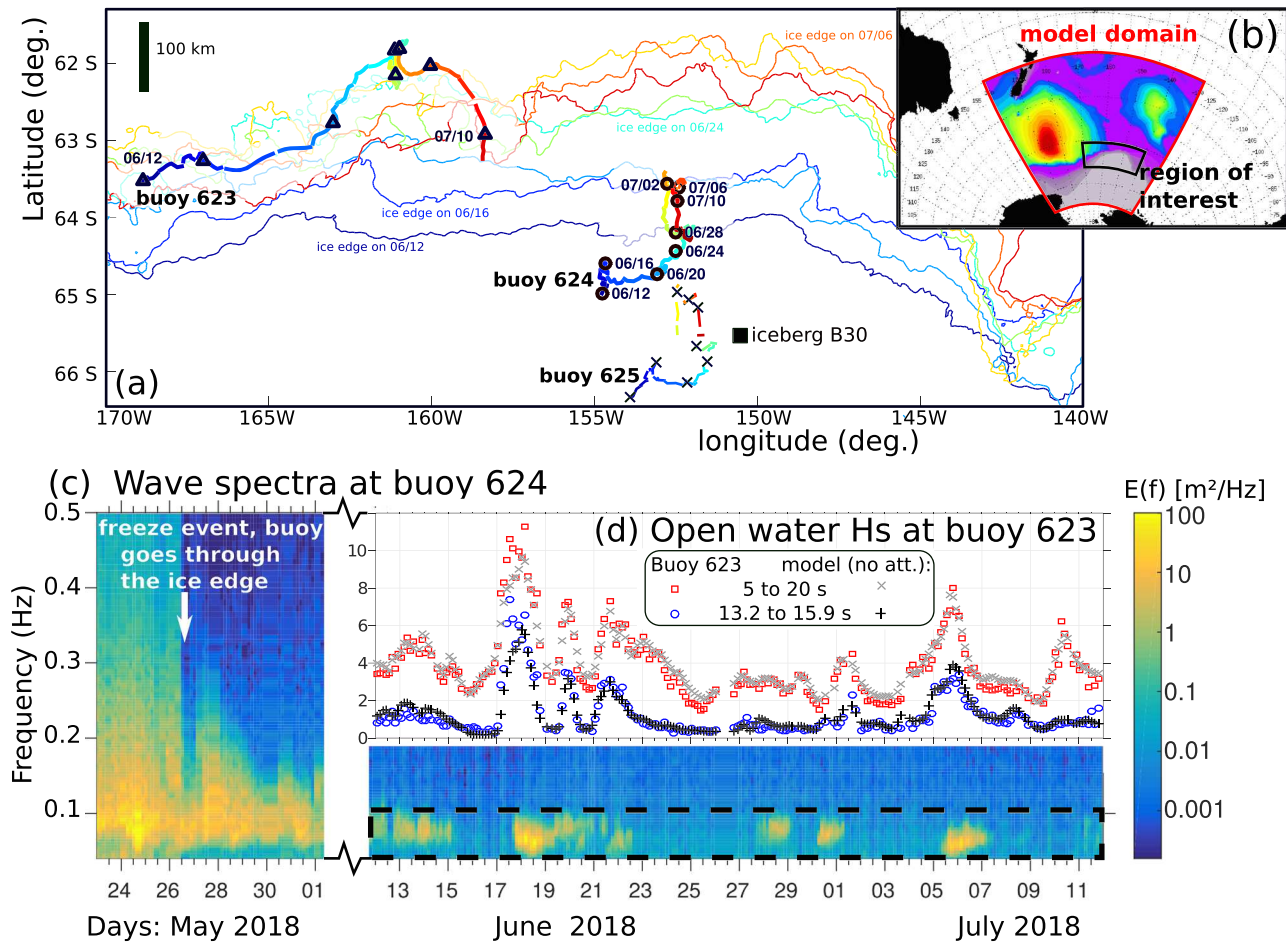


Figure 1. (a) Positions of the ice edge, defined as the 15% ice concentration contour, every 4 days from 12 June to 10 July 2018, and positions of three minibuys, Numbers 623 (triangles in open water), 624 (circles in the ice), and 625 (crosses, further in the ice). (b) Geographical context and domain of the numerical wave model used in section 3. The black rectangle corresponds to the region shown in (a), the colors show simulated significant wave heights from 0 to 10 m on 4 July at 12:00 UTC. (c) Wave energy spectra at Buoy 624. (d) Time series of measured and modeled wave height at the Open Water Buoy 623 for period ranges 5 to 20 s and 13.2 to 15.9 s. See also supporting information Movie S1.

observed sudden drop in wave attenuation when ice is broken by waves (Collins et al., 2015). Here the floe sizes are constrained by Synthetic Aperture Radar (SAR) imagery.

2. Measured Wave Properties and Sea Ice Conditions

Freely drifting wave buoys (Drazen et al., 2016) were deployed in the Southern Ocean in 2018 and advected into advancing sea ice. Figure 1a shows the trajectories of three buoys numbered 623, 624, and 625. Successive positions of the ice edge, defined as the 15% ice concentration contour, are estimates from the Advanced Microwave Scanning Radiometer 2 (AMSR2, Spreen et al., 2008).

Buoy 624 measured a typical wave signal as shown in Figure 1c. High wave frequencies (above 0.3 Hz) vanish once the buoy is a few kilometers into the ice on 26 May. This attenuation is similar to other measurements obtained during the formation of meter-scale rafts of ice known as pancakes (Thomson et al., 2018). Frequencies between 0.10 and 0.30 Hz gradually disappear as the buoy gets deeper into the ice, 80 km from the ice edge on 12 June. This evolution is presumably associated with the progressive welding of pancakes into much larger floes forming solid plates that can extend over kilometers. After 12 June, only frequencies under 0.1 Hz are episodically recorded as the ice margin continues to extend further offshore reaching a distance of 150 km from 624 by 24 June. Wave energy exceeds the instrument noise floor during seven events observed by the buoy, each of which is associated with a storm (Figure 2a). Buoy 625 kept a nearly

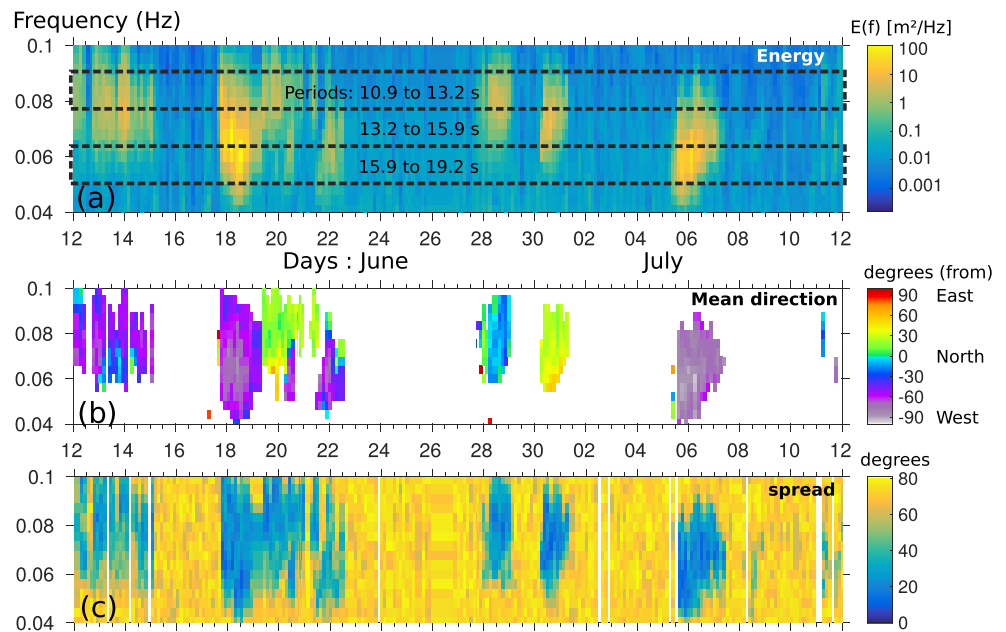


Figure 2. Wave properties measured by Buoy 624 as a function of time and frequency. (a) Energy spectrum, with dotted boxes around the short and long period ranges used in Figure 4, (b) Mean directions, shown when the energy is above -10 dB, avoiding random noise for low energies. (c) Directional spread.

constant distance south of 624, 120 km further into the ice field, until its trajectory crosses Iceberg B30 on 14 July. This 30 km long iceberg is clearly visible in all the AMSR2 images as it cuts a wake of open water in the sea ice. Before 13 July, Buoy 623 was out of the ice, providing measurements representative of open water. A numerical model simulation without ice attenuation shows good agreement with these measurements (Figure 1d). This model is used to quantify the time delay and dispersion due to propagation from open water (Buoy 623) into the ice (Buoys 624 and 625). The difference between the model and observations can then be attributed to wave-ice interaction processes.

The wave height observed within the ice is not a simple function of the open water measurements, as shown in Figure 1d. The attenuation from open water to Buoy 624 depends on the wave frequency and direction. Attenuation is stronger for higher frequencies. Attenuation is also stronger when waves travel a longer distance under the ice, namely, when their directions are more oblique relative to the ice edge (e.g., from the west, in gray-purple colors on 4–7 July, Figure 2b). The buoy measures narrow directional distributions with spreads under 20° (blues in Figure 2c) as soon as the energy level exceeds $0.1 \text{ m}^2/\text{Hz}$. The measured waves are thus similar to open ocean swell with long crests and a narrow range of propagation directions.

We now turn to Sentinel-1 radar imagery for information on ice properties. These SAR images were analyzed for two types of features (Figure 3).

First we determined the presence (blue symbols) or absence (red symbols) of leads. Leads are straight features at the boundaries of large-scale floes that may correspond to an ice-free surface, which appear as dark bands or that can refreeze and appear bright due to the presence of frost flowers. When leads are visible, the diameters of floes exceed 1 km and waves have not been able to break the ice. In the absence of leads, it is expected that ice is broken into small floes and their differential advection yields a horizontally uniform brightness. The second type of feature is wave patterns. Images numbered 4–6 acquired on 5 July clearly show a wave field propagating from the west, with a dominant wavelength around 400 m that is reduced to 270 m in Images 11, 12, and 14 acquired on 6 July. Estimated wave heights (Ardhuin et al., 2017) range from 0.7 to 2.5 m. Much fainter wave patterns are also visible in Images 2, 3, and 7. All these wave features are long crested except in Image 8 where ring waves are observed in probable association with reflections off an iceberg. The radar imagery acquired around the trajectories of the buoys thus confirms the penetration, 200 km inside the ice, of long-crested waves with heights on the order of 1 m. Also, we interpret the disappearance of leads toward the ice edge on 5 and 6 July as the result of ice breakup by wave action.

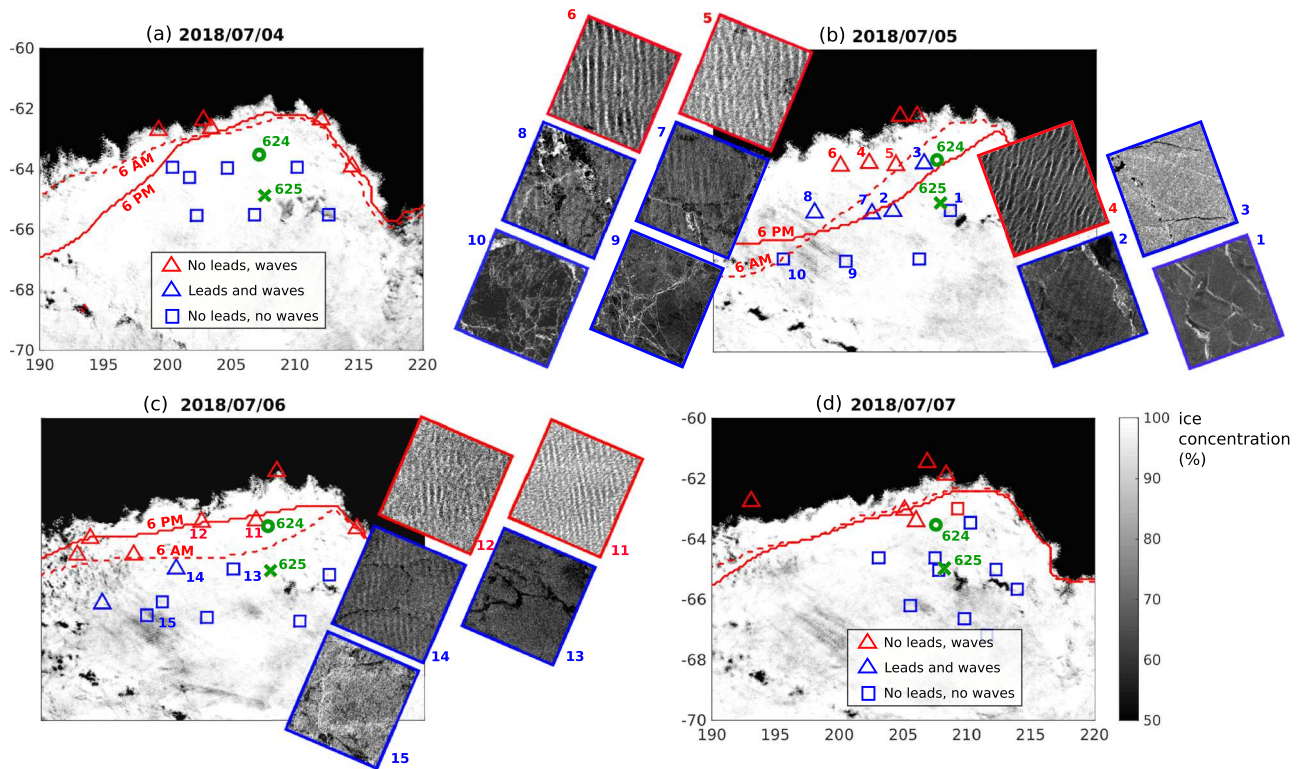


Figure 3. Daily maps of ice concentrations (from AMSR2-ASI, as provided by University of Bremen), buoy positions and locations of Sentinel 1 Wave Mode SAR imagery classified by the presence of leads and waves, through a storm event on (a) 4 July, (b) 5 July, (c) 6 July, and (d) 7 July. Each SAR image is represented by a blue symbol if leads are detected, red if no lead is detected, triangles if waves are visible, squares otherwise. For some of the images, numbered 1 to 15, subsets of the SAR images are also shown. Each subset is 5 km by 5 km, and full images are shown in Figures S1–S15. Finally, the contour of maximum floe diameter $D_{\max} = 300$ m, as estimated from the model run using anelastic dissipation, is shown with a dashed line at 6 a.m. and solid line at 6 p.m. marking the extent of the regions where ice is broken by waves in the model.

3. Interpretation Using a Wave Attenuation and Ice Breakup Mode

The magnitude and a plausible cause of wave attenuation will now be examined with a numerical wave model, based on version 6.05 of the WAVEWATCH III modeling framework (*The WAVEWATCH III*® Development Group, 2019, hereinafter WW3), that is constrained by these ice observations. We consider three model simulations that differ only in their parameterizations of wave-ice interactions:

- A simple “no-attenuation” simulation in which the effect of the ice is limited to shutting off the generation of waves by wind forcing and dissipation associated with wave breaking. The difference between the measurements and the “no-attenuation” run provides an estimate of the ice-induced attenuation.
- A scattering + viscous basal friction (“S1V1” for short) in which the scattering coefficient is determined by the ice thickness and maximum floe size following Williams et al. (2013) with the addition of back-scattering (so that the scattering term conserves energy) and viscous dissipation taken from Liu and Mollo-Christensen (1988) with the viscosity taken to be the molecular viscosity of sea water at the freezing point. Our scattering term conserves wave energy which is isotropically redistributed as discussed in Boutin et al. (2018). Scattering strength is based on the normal reflection of waves traveling from the open ocean under a semi-infinite ice floe with a straight boundary (Williams et al., 2013).
- An anelastic dissipation based on known microscopic rheological properties of dislocations in ice crystals (Cole, 2020; Cole et al., 1998), adapted by Boutin et al. (2018) to represent the dissipation of waves when floes with diameters larger than half the wavelength are flexing. This parameterization is combined with viscous basal friction and scattering, with the scattering coefficient reduced by a factor of 5.

Apart from the differences in parameterizations, the common features of the three model simulations reported here are a spatial resolution of 0.1° in latitude and 0.2° in longitude, forced at the boundaries

(red line in Figure 1b) by a 0.5° global wave model. Wind forcing is provided by the European Center for Medium Range Weather Forecasts (ECMWF) operational analyses and forecasts. Ice concentration was provided by AMSR2 with a correction designed to limit the errors caused by atmospheric water vapor (Gloersen & Cavalieri, 1986): All concentrations above 70% was set to 100%. Based on climatology data, the ice thickness was set to a constant 0.77 m. Given our focus on wave periods longer than 10 s, we neglected the effect of ice on wave dispersion (Collins et al., 2018). This is discussed in the supporting information. The model uses 24 directions and an exponential frequency grid from 0.037 to 1 Hz.

The ice flexural strength σ_c was adjusted to obtain a position of the breakup front consistent with SAR imagery, as shown in Figure 3, giving $\sigma_c = 0.6$ MPa.

In all cases the maximum floe size diameter is estimated based on the expected local maximum flexural strength over the model time step of 600 s (Boutin et al., 2018). This floe size only has an impact on wave dissipation rate in the case of the anelastic simulation.

We also note that other wave-ice interaction effects have been investigated in other studies (Squire, 2020), including ice floe collisions (Herman et al., 2019) or the breaking of steep waves over ice floes (Toffoli et al., 2015). Although these processes are reasonably important right at the ice edge, we expect them to play only a minor role overall because they are typically nonlinear with higher relative dissipation for higher waves, hence leading to a shorter attenuation distance for steeper ocean waves. This is not consistent with available large-scale observations that show a constant or weaker attenuation for steeper waves (Meylan et al., 2014; Stopa et al., 2018), and we thus have not considered these processes here.

Modeled wave parameters are compared to the buoy measurements in Figure 4. A detailed analysis of the shape of wave spectra is performed in the supporting information; see Figures S16–S21. Starting with the directional spread in Figure 4a, measurements during wave events are only slightly larger than those modeled without ice attenuation. In contrast, the modeled spread is much larger than observed values when scattering is a dominant term in the attenuation (run S1V1). Reducing the spread to levels comparable to measured values requires a reduction of the scattering coefficient by at least a factor of 5, as in the “anelastic” simulation. This reduced scattering requires stronger dissipation processes to explain the measured wave height attenuation. This attenuation is estimated as the ratio between the “no-attenuation” simulation and the measured height, and it varies dramatically in time and across frequencies. Some of these variations are caused by different offshore directions (Figure 2b). Still, for similar wave directions, the observed attenuation varies from 80% to 20% between 20 and 30 June (purple arrows in Figure 4c). The gradual variation of wave attenuation in the S1V1 simulation is markedly different from observations which exhibit a sharp cutoff after each wave event such as on 2 or 8 July when no wave energy is measured at Buoy 624 (Figures 4b–4d). The anelastic simulation reproduces that effect which, in the model, is due to displacement of the “breakup front” shown with red contours in Figure 3. When Buoy 624 is far from the “breakup front,” the distance traveled by waves across unbroken ice is large and the attenuation is very strong. In contrast, when the ice is broken up closer to the buoy, the attenuation is much less with an overall wave height attenuation by ice as low as 20%.

The anelastic model scenario presented above is not a unique solution. We assumed an ice thickness $h = 0.77$ m and adjusted the ice flexural strength to $\sigma_c = 0.6$ MPa in order to obtain a spatial extent of broken ice consistent with SAR imagery. Because the ice breakup condition in the model is set by a maximum stress that is proportional to $\sigma_c h^2$, the same results may be obtained by increasing h by a factor a and reducing σ_c by a factor a^2 . Likewise, the magnitude of the anelastic dissipation is controlled by the compliance of the relaxation of dislocations δ and the number of dislocations per unit area (Cole, 2020). Since the wave dissipation rate is proportional to $h^3 \delta$, any change in h can be compensated with a change of δ to give the same wave evolution. Conversely, assuming that δ and σ_c are well constrained, it is possible to estimate the ice thickness from SAR imagery using either wave heights and periods at the breakup front or the attenuation of waves in unbroken ice.

For such applications a more realistic dissipation model may be needed. Indeed, the present parameterization tends to overestimate the dissipation of frequencies above 0.085 Hz, as shown in supporting information Figures S16–S20. One possible reason for this model error is the neglected effect of ice in the dispersion relation (Robinson & Palmer, 1990), but other dissipative processes may be involved, including flow in brine

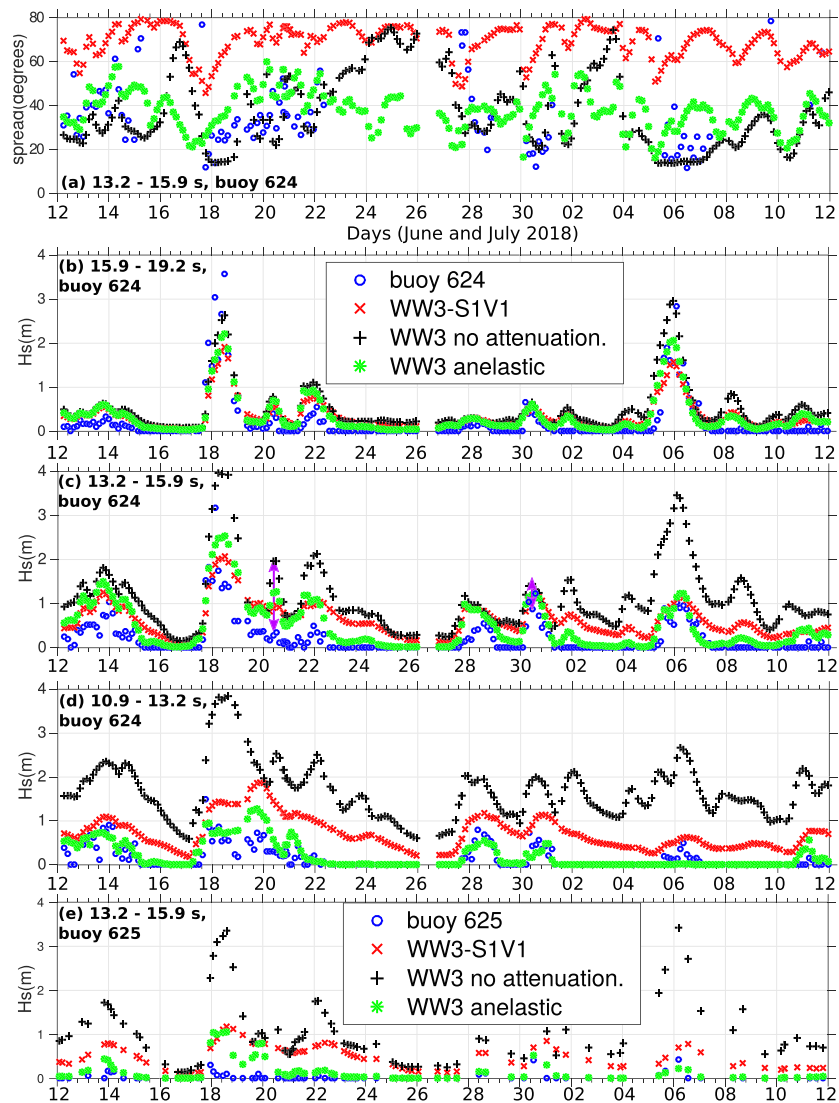


Figure 4. Time series of measured and modeled (a) directional spread and (b–e) wave heights for the ranges of wave periods shown in Figure 2a. The model results are shown for the three different parameterizations of wave-ice interactions. Purple arrows in (c) point to markedly different attenuation rates, 80% on 20 June and 20% on 30 June.

pockets during ice deformation and viscous effects in ice deformation (Cole, 2020; Marchenko & Cole, 2017; Meylan et al., 2018).

4. Conclusions

As storms passed over the open ocean, we measured waves in the ice with narrow directional spreads that are not compatible with existing parameterizations of wave scattering by ice floes. Instead, dissipation associated with ice flexure is a plausible explanation for the previously observed nonlinear wave attenuation (Stopa et al., 2018) with weaker attenuation for higher waves. This dissipation provides a transition from a nonbroken and highly dissipative flexing ice field to one which is fragmented into small floes with weak attenuation, consistent with our wave and ice observations. This new paradigm also has consequences on how the waves impact the ice. In particular, a dissipation-dominated attenuation concentrates the wave-induced push to the ice around the ice breakup front. In the melting season, the waves may have a more lasting impact as large floes may not reform after each storm, allowing breakup to progress further with the next storm.

Data Availability Statement

Buoy data have been uploaded to the UC San Diego Library Digital Collections (<https://doi.org/10.6075/J0V40SM5>). Level-1 SAR wave mode data were provided by the European Space Agency and can be viewed online (at <http://www.ifremer.fr/datavore/exp/dvor/\#/s1quicklook>); their processing supported by Sentinel-1 A Mission Performance Center (Contract 4000107360/12/I-LG). Finally, model simulations are available online (at <http://tiny.cc/wavesinice>).

Acknowledgments

We thank the New Zealand Navy for buoy deployments and the EU/ESA Copernicus program for the acquisition of SAR imagery. The analysis was supported by ONR under grant N00014-17-1-2402. Comments from anonymous reviewers and discussions with David Cole are gratefully acknowledged.

References

- Ardhuin, F., Chapron, B., Collard, F., Smith, M., Stopa, J., Thomson, J., et al. (2017). Measuring ocean waves in sea ice using SAR, imagery: A quasi-deterministic approach evaluated with Sentinel-1 and in situ data. *Remote Sensing of Environment*, *189*, 211–222. <https://doi.org/10.1016/j.rse.2016.11.024>
- Ardhuin, F., Sutherland, P., Doble, M., & Wadhams, P. (2016). Ocean waves across the Arctic: Attenuation due to dissipation dominates over scattering for periods longer than 19 s. *Geophysical Research Letters*, *43*, 5775–5783. <https://doi.org/10.1002/2016GL068204>
- Boutin, G., Ardhuin, F., Dumont, D., Sévigny, C., & Girard-Ardhuin, F. (2018). Floe size effects on wave-ice interactions: Theoretical background, implementation and applications. *Journal of Geophysical Research: Oceans*, *123*, 4779–4805. <https://doi.org/10.1029/2017JC013622>
- Cole, D. M. (2020). On the physical basis for the creep of ice: The high temperature regime. *Journal of Glaciology*, *66*(257), 401–414. <https://doi.org/10.1017/jog.2020.15>
- Cole, D. M., Johnson, R. A., & Durell, G. D. (1998). Cyclic loading and creep response of aligned first-year sea ice. *Journal of Geophysical Research*, *103*(C10), 21,751–21,758.
- Collins, C., Doble, M., Lund, B., & Smith, M. (2018). Observations of surface wave dispersion in the marginal ice zone. *Journal of Geophysical Research: Oceans*, *123*, 2851–2866. <https://doi.org/10.1002/2017JC013693>
- Collins, C., Rogers, W. E., Marchenko, A., & Babanin, A. V. (2015). In situ measurements of an energetic wave event in the Arctic marginal ice zone. *Geophysical Research Letters*, *42*, 1863–1870. <https://doi.org/10.1002/2015GL063063>
- Doble, M. J., & Bidlot, J.-R. (2013). Wave buoy measurements at the Antarctic sea ice edge compared with an enhanced ECMWF WAM: Progress towards global waves-in-ice modelling. *Ocean Modelling*, *70*, 166–173. <https://doi.org/10.1016/j.ocemod.2013.05.012>
- Drazen, D., Merrill, C., Gregory, S., Fullerton, A., Terrill, E., & de Paolo, T. (2016). Interpretation of in-situ ocean environmental measurements, Proc. 31st Symp. on Naval Hydrodynamics.
- Gloersen, P., & Cavalieri, D. J. (1986). Reduction of weather effects in the calculation of sea ice concentration from microwave radiances. *Journal of Geophysical Research*, *91*(C3), 3913–3919.
- Herman, A., Cheng, S., & Shen, H. H. (2019). Wave energy attenuation in fields of colliding ice floes Part 2: A laboratory case study. *The Cryosphere*, *13*, 2911–2914. <https://doi.org/10.5194/tc-13-2901-2019>
- Kohout, A. L., Williams, M. J. M., Dean, S. M., & Meylan, M. H. (2014). Storm-induced sea-ice breakup and the implications for ice extent. *Nature*, *509*, 604–607. <https://doi.org/10.1038/nature13262>
- Kohout, A. L., Williams, M. J. M., Toyota, T., Lieser, J., & Hutchings, J. (2016). In situ observations of wave-induced sea ice breakup. *Deep Sea Research Part II*, *131*, 22–27. <https://doi.org/10.1016/j.dsr2.2015.06.010>
- Liu, A. K., & Mollo-Christensen, E. (1988). Wave propagation in a solid ice pack. *Journal of Physical Oceanography*, *18*, 1702–1712.
- Marchenko, A., & Cole, D. (2017). Three physical mechanisms of wave energy dissipation in solid ice. In *Proceedings of the 24th International Conference on Port and Ocean Engineering under Arctic Conditions* (pp. 1378–1381). Busan, Korea: National Research Council of Canada.
- Meylan, M. H., Bennetts, L. G., & Kohout, A. L. (2014). In situ measurements and analysis of ocean waves in the Antarctic marginal ice zone. *Geophysical Research Letters*, *41*, 5046–5051. <https://doi.org/10.1002/2014GL060809>
- Meylan, M. H., Bennetts, L. G., Mosig, J. E. M., Rogers, W. E., Doble, M. J., & Peter, M. A. (2018). Dispersion relations, power laws, and energy loss for waves in the marginal ice zone. *Journal of Physical Oceanography*, *123*, 3322–3335. <https://doi.org/10.1002/2018JC013776>
- Robinson, N. J., & Palmer, S. C. (1990). A modal analysis of a rectangular plate floating on an incompressible liquid. *Journal of Sound and Vibration*, *142*(3), 452–460. [https://doi.org/10.1016/0022-460X\(90\)90661-I](https://doi.org/10.1016/0022-460X(90)90661-I)
- Spreen, G., Kaleschke, L., & Heygster, G. (2008). Sea ice remote sensing using AMSR-E 89-GHz. *Journal of Geophysical Research*, *113*, C02S03. <https://doi.org/10.1029/2005JC003384>
- Squire, V. A. (2020). Ocean wave interactions with sea ice: A reappraisal. *Annual Review of Fluid Mechanics*, *52*, 37–60. <https://doi.org/10.1146/annurev-fluid-010719-060301>
- Stopa, J. E., Ardhuin, F., & Girard-Ardhuin, F. (2016). Wave climate in the Arctic 1992–2014: Seasonality and trends. *The Cryosphere*, *10*, 1605–1629. <https://doi.org/10.5194/tc-10-1605-2016>
- Stopa, J. E., Sutherland, P., & Ardhuin, F. (2018). Strong and highly variable push of ocean waves on Southern Ocean sea ice. *Proceedings of the National Academy of Sciences of the United States of America*, *115*(23), 5861–5865. <https://doi.org/10.1073/pnas.1802011115>
- Sutherland, P., & Dumont, D. (2018). Marginal ice zone thickness and extent due to wave radiation stress. *Journal of Physical Oceanography*, *48*, 1885–1901. <https://doi.org/10.1175/JPO-D-17-0167.1>
- The WAVEWATCH III® Development Group (2019). User manual and system documentation of WAVEWATCH III® version 6.07 (Tech. Note 333). College Park, MD, USA: NOAA/NWS/NCEP/MMAB.
- Thomson, J., Ackley, S., Girard-Ardhuin, F., Ardhuin, F., Babanin, A., Boutin, G., et al. (2018). Overview of the Arctic sea state and boundary layer physics program. *Journal of Geophysical Research: Oceans*, *123*, 8674–8687. <https://doi.org/10.1002/2018JC013766>
- Toffoli, A., Bennetts, L. G., Meylan, M. H., Cavaliere, C., Alberello, A., Elsnab, J., & Monty, J. P. (2015). Sea ice floes dissipate the energy of steep ocean waves. *Geophysical Research Letters*, *42*, 8547–8554. <https://doi.org/10.1002/2015GL065937>
- Wadhams, P. (1988). Winter observations of iceberg frequencies and sizes in the South Atlantic Ocean. *Journal of Geophysical Research*, *93*, 3583–3590.
- Williams, T. D., Bennetts, L. G., Squire, V. A., Dumont, D., & Bertino, L. (2013). Wave-ice interactions in the marginal ice zone. Part 1: Theoretical foundations. *Ocean Modelling*, *70*, 81–91. <https://doi.org/10.1016/j.ocemod.2013.05.010>

Supporting Information for "Ice break-up controls dissipation of wind-waves across Southern Ocean sea ice"

Fabrice Ardhuin¹, Mark Otero¹, Sophia Merrifield¹, Antoine Grouazel², and

Eric Terrill¹

¹Scripps Institution of Oceanography, La Jolla, California

²Univ. Brest, CNRS, IRD, Ifremer, Laboratoire d'Océanographie Physique et Spatiale (LOPS), IUEM, Brest, France

Contents of this file

1. Movie S1
2. Figures S1 to S15

Introduction This Supporting information contains a movie that complements Figure 1 and helps visualizing the position of the buoys relative to the ice edge in the context of the measured storms. The supplementary figures S1-S15 provide a more detailed view of the ice and wave features observed on July 5 and 6, complementing figure 4.

Movie S1. Position of the three buoys 623, 624 and 625 in the context of the evolving sea ice concentration field as estimated from the Advanced Microwave Scanning Radiometer 2, processed by the University of Bremen (?, ?). Maximum floe size contour $D_{\max} = 300$ m and wave heights and mean directions are taken from the the "Anelastic" model run.

Figures S1-S15. Quicklooks of SAR images labeled 1-15 in Fig. 3. These can be obtained from <http://www.ifremer.fr/datavore/exp/dvor/##/s1quicklook>. Images are displayed in the acquisition geometry with the range direction on the x -axis and the azimuth (satellite track) direction on the y -axis, and subsampled to make a 600 by 600 pixel image with a resolution of 35 m from the original Level 1 product that has a resolution of 4 m. The grey scale representing radar backscatter after SAR processing is automatically adjusted to linearly cover the 1st to 99th percentiles of the image intensity. The mean value μ is indicated on each figure. The samples shown in Fig. 3 were rotated to have the North direction up.

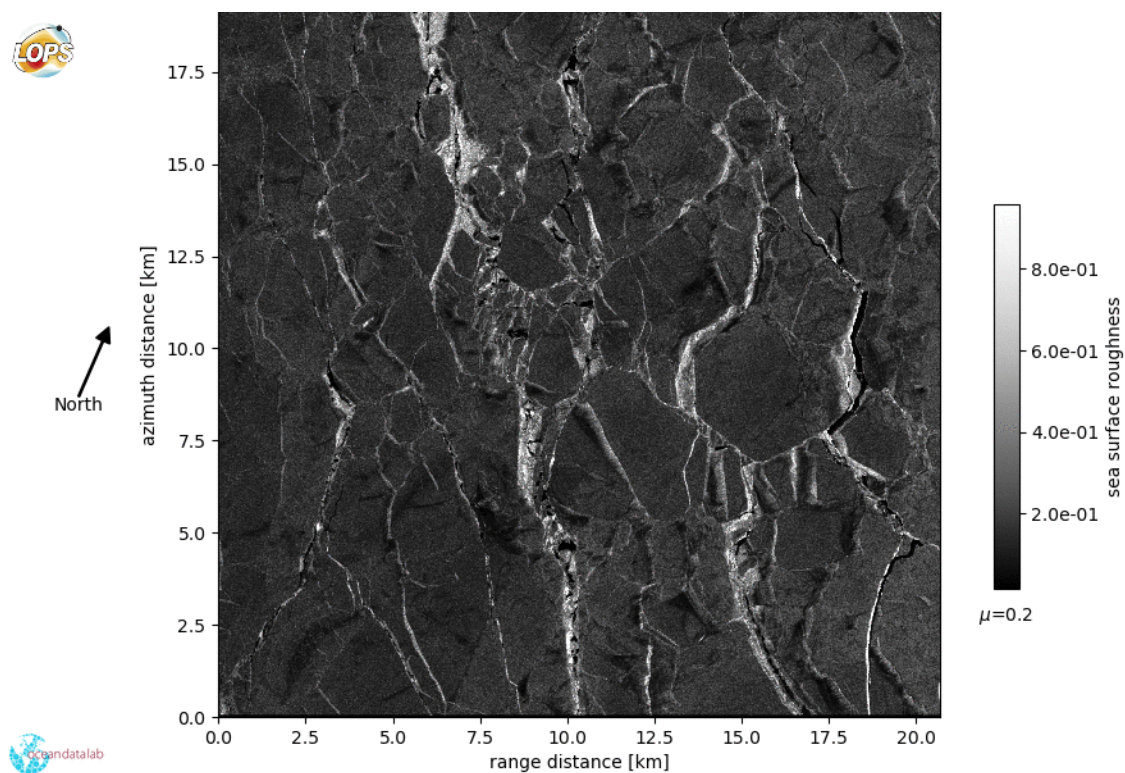


Figure S1: acquired 2018/07/05 at 06:01:08

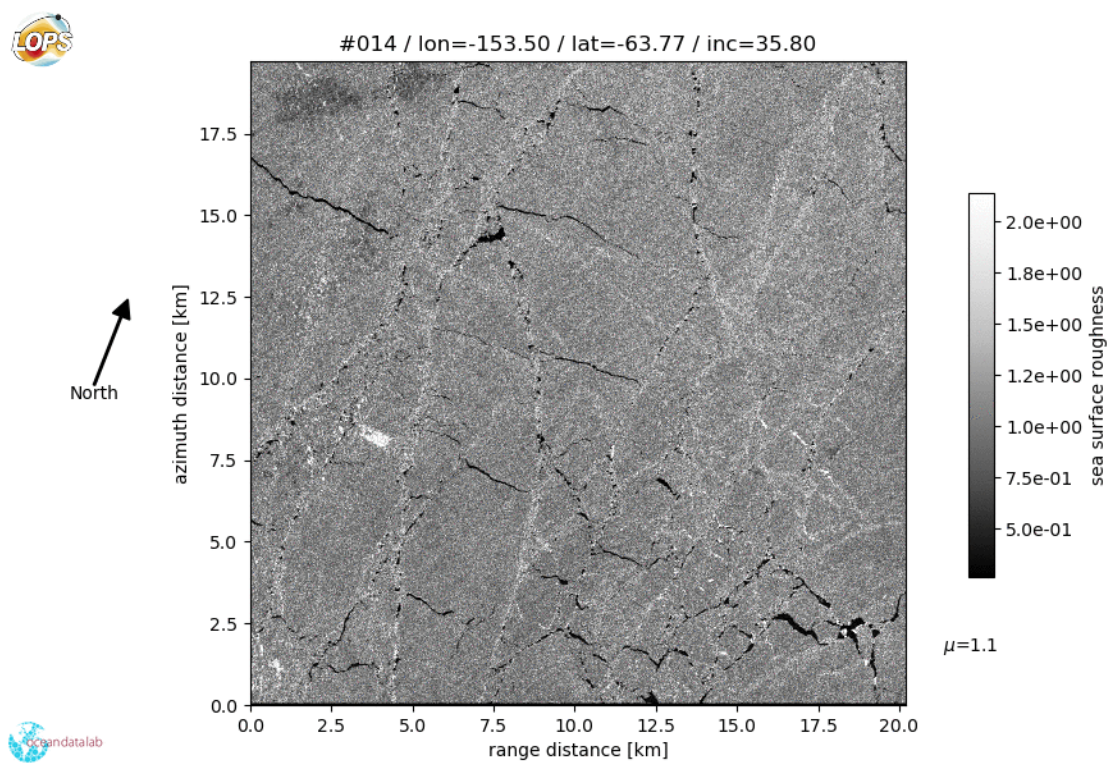
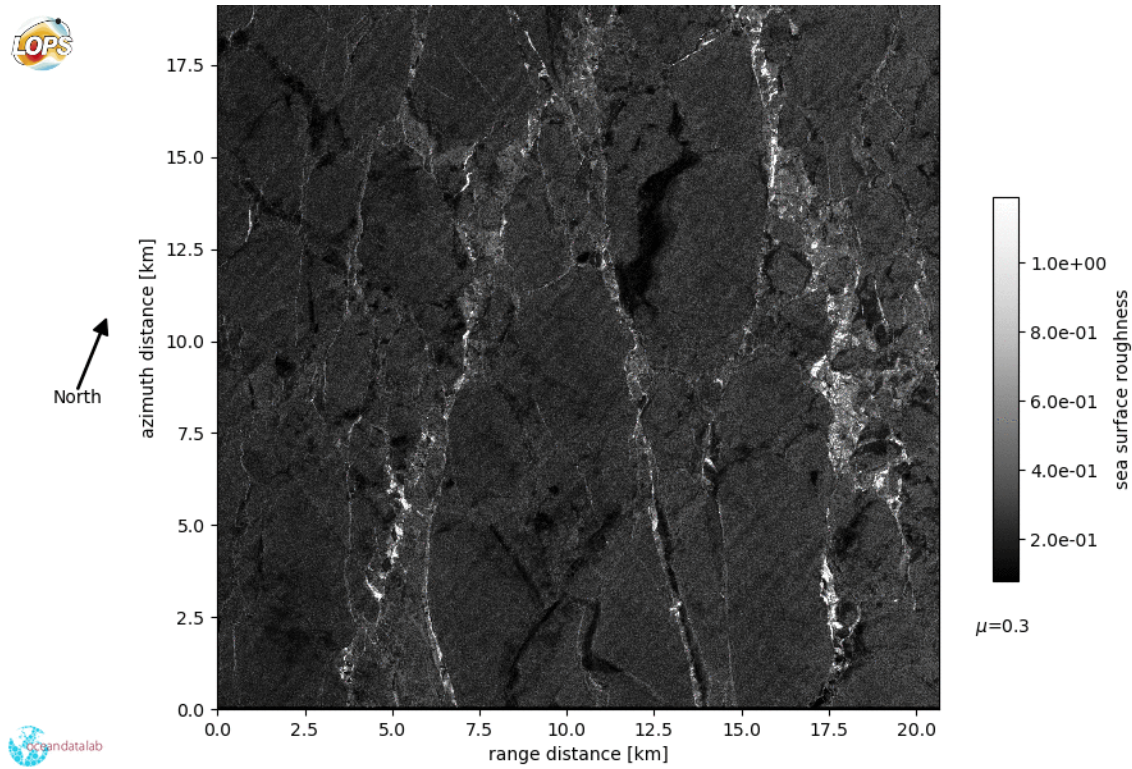


Figure S3: acquired by Sentinel 1B on 2018/07/05 at 06:01:52

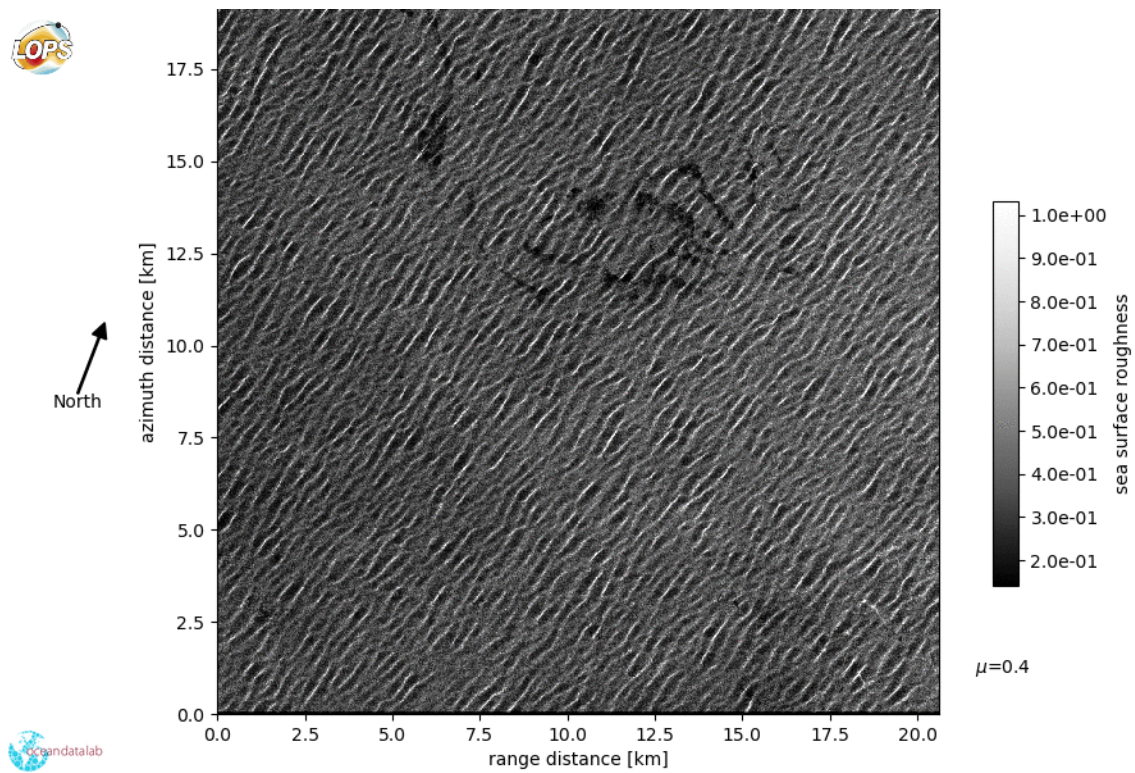


Figure S4: acquired by Sentinel 1B on 2018/07/05 at 06:02:07

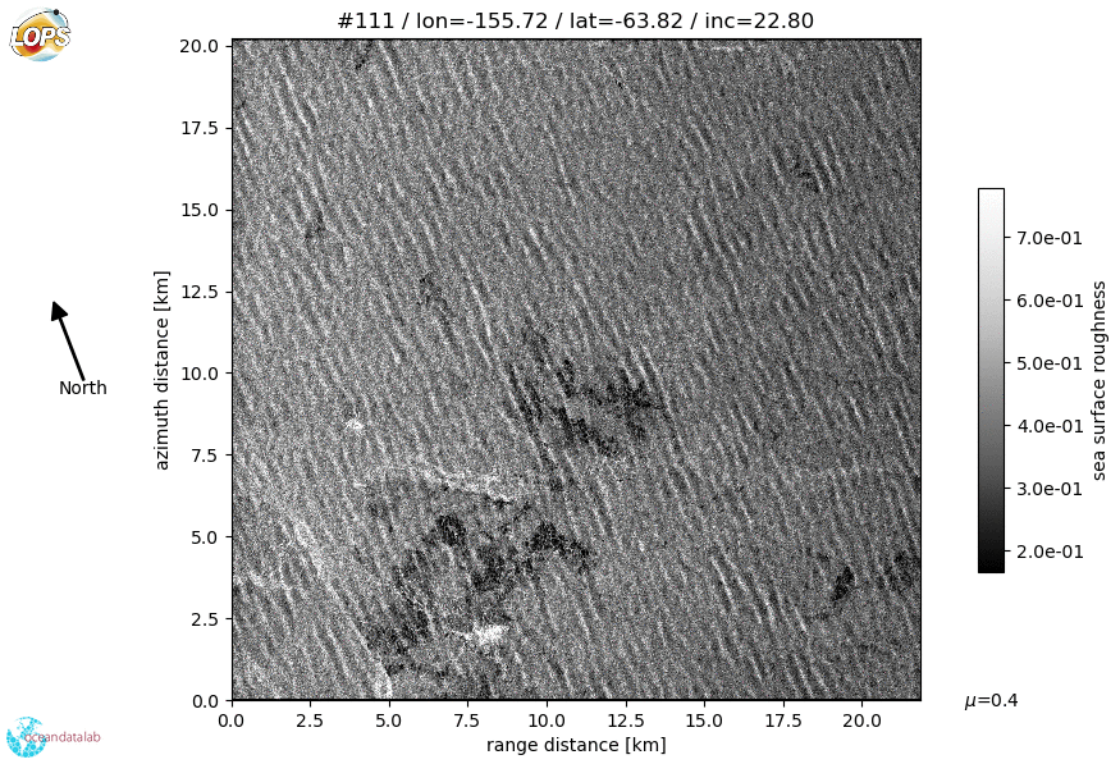
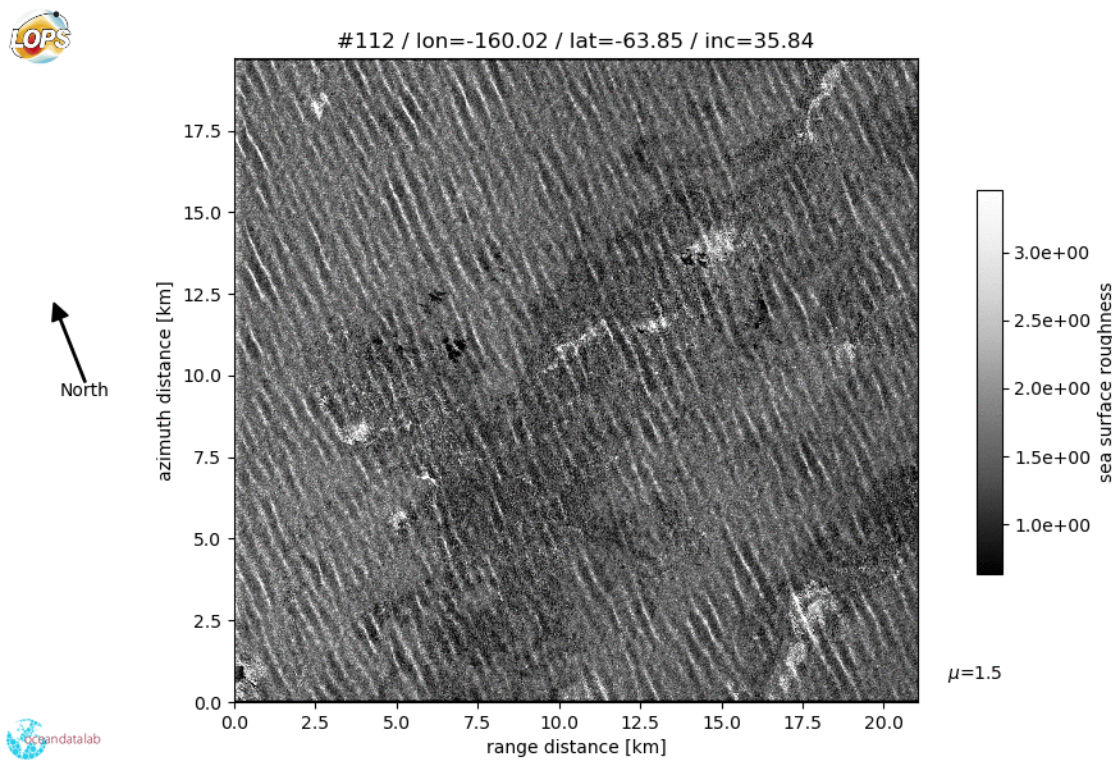


Figure S5: acquired by Sentinel 1A on 2018/07/05 at 14:52:37



May 11, 2020, 11:13pm

Figure S6: acquired by Sentinel 1A on 2018/07/05 at 14:52:52

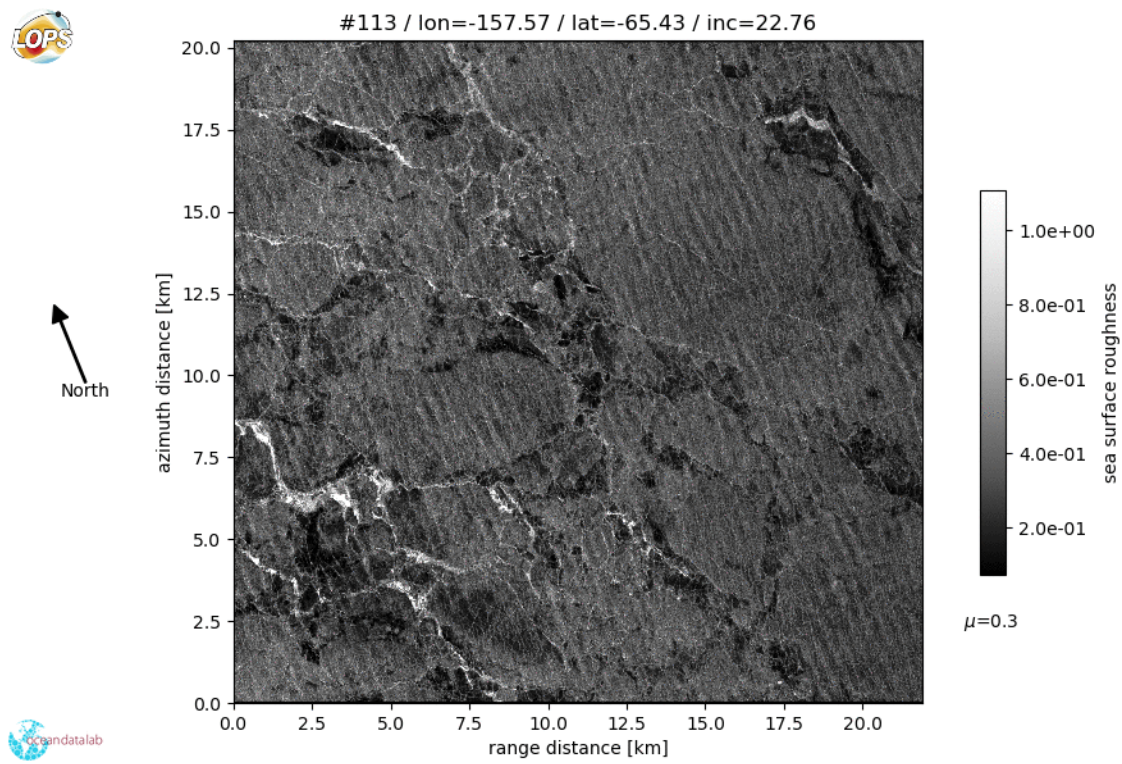


Figure S7: acquired by Sentinel 1A on 2018/07/05 at 14:53:06

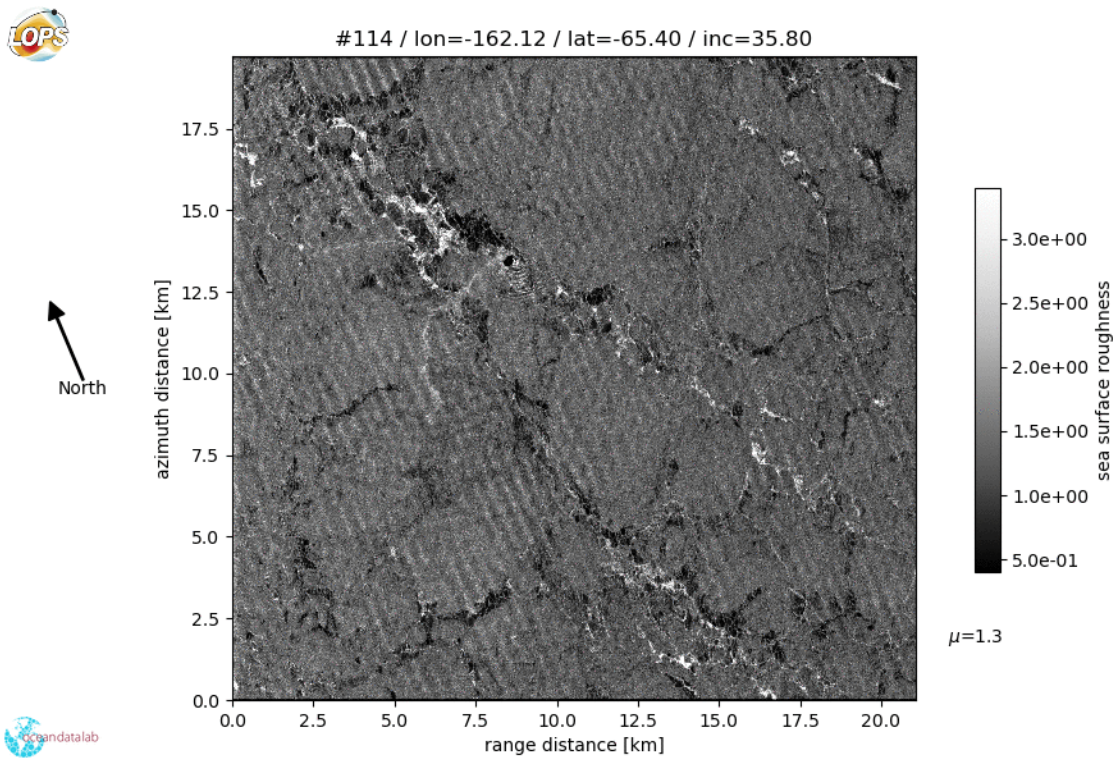
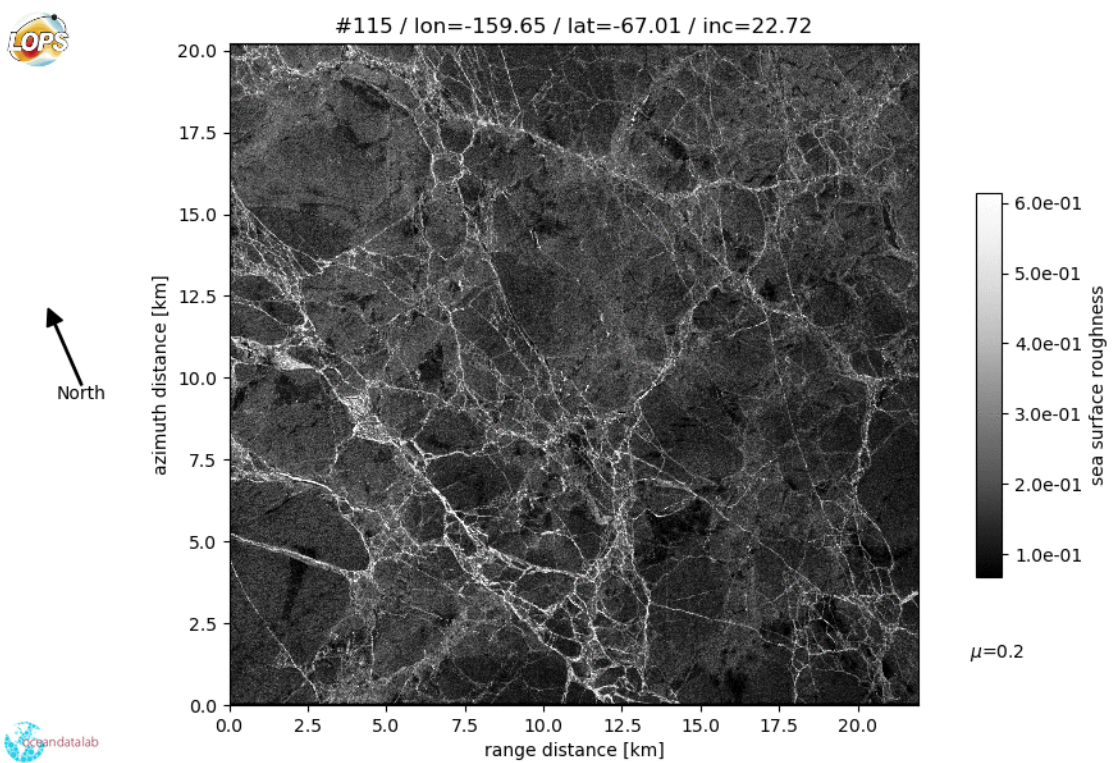


Figure S8: acquired by Sentinel 1A on 2018/07/05 at 14:53:21



May 11, 2020, 11:13pm

Figure S9: acquired by Sentinel 1A on 2018/07/05 at 14:53:36

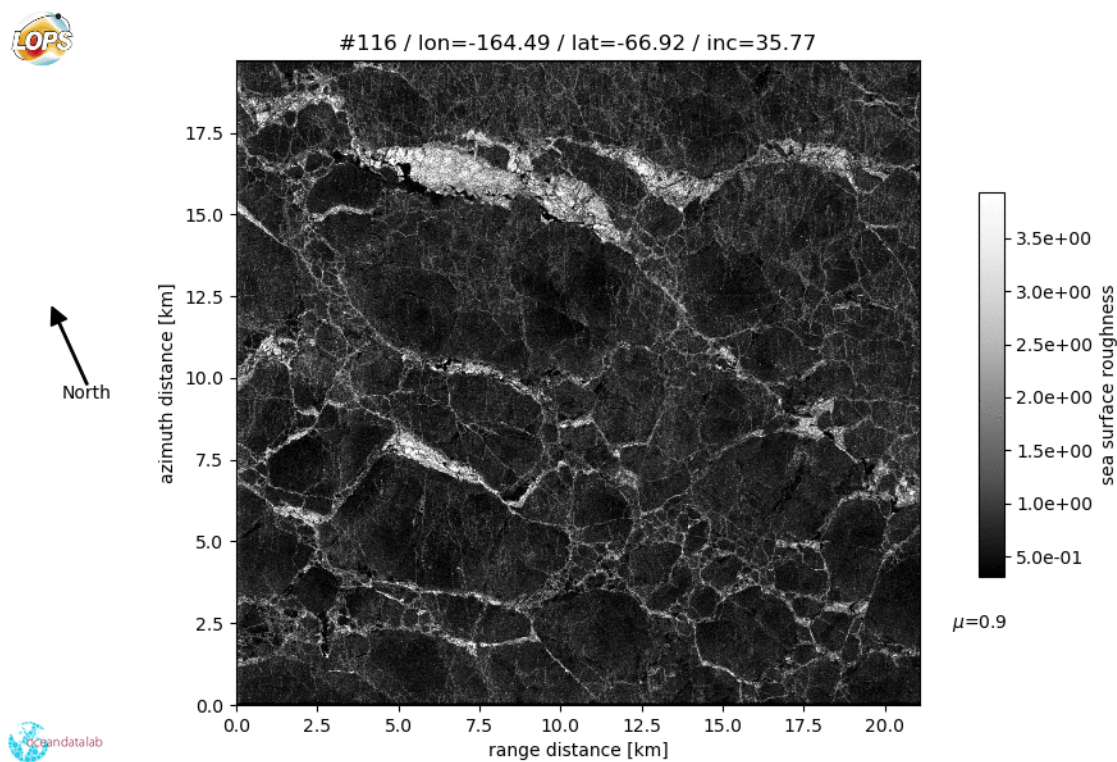


Figure S10: acquired by Sentinel 1A on 2018/07/05 at 14:53:50

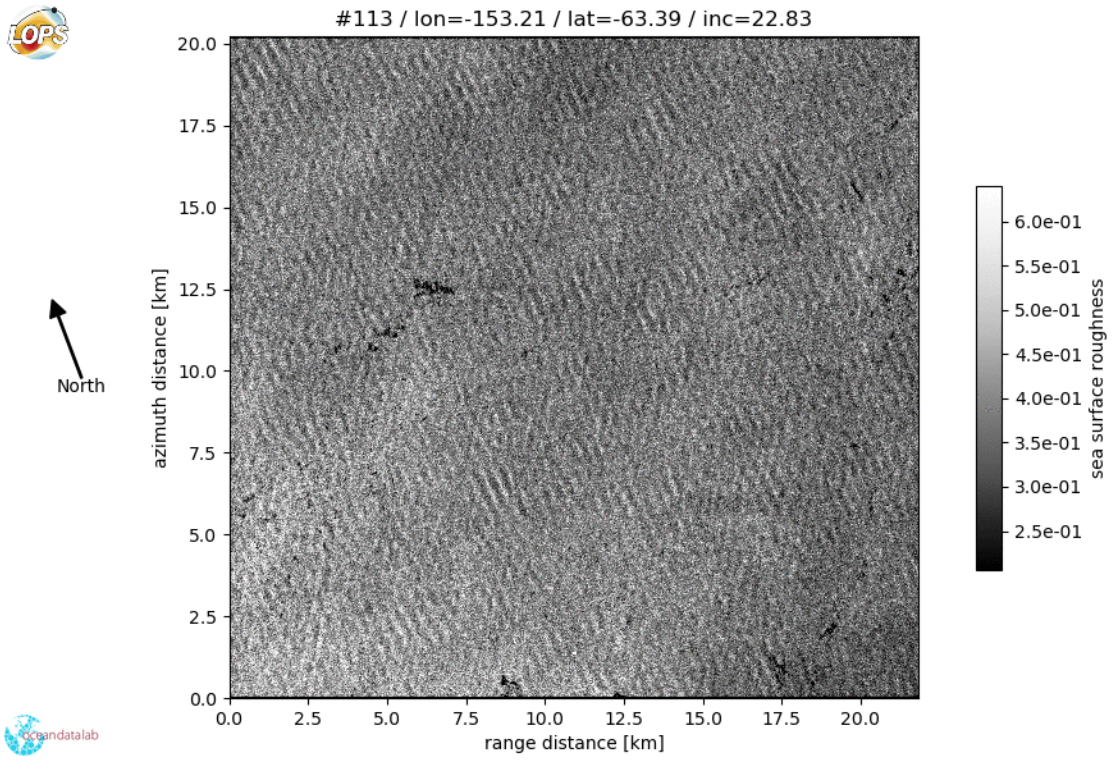
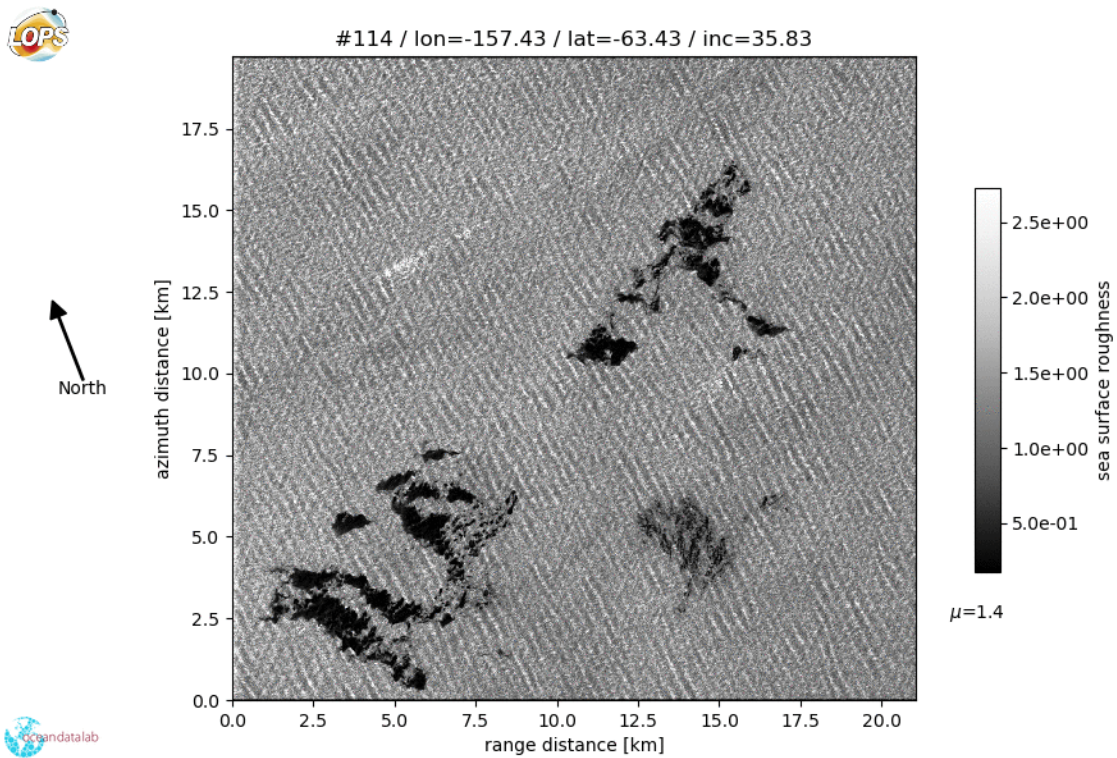


Figure S11: acquired by Sentinel 1B on 2018/07/06 at 14:43:34



May 11, 2020, 11:13pm

Figure S12: acquired by Sentinel 1B 2018/07/06 at 14:43:49

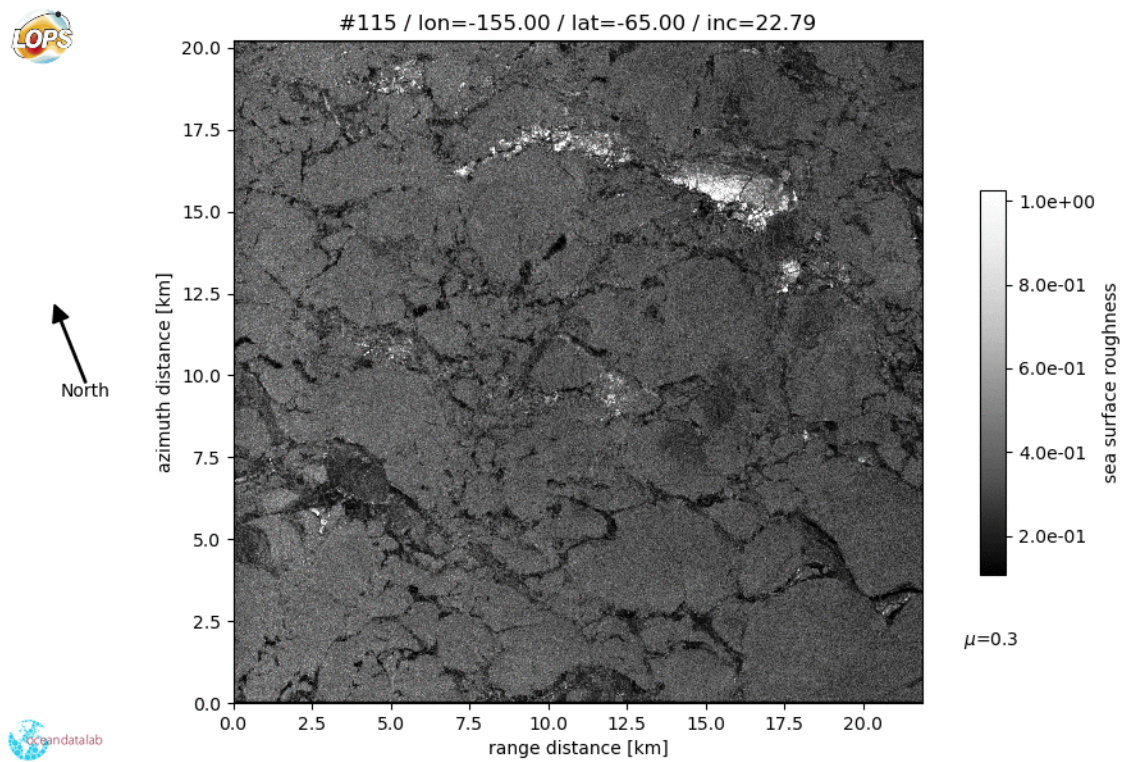


Figure S13: acquired by Sentinel 1B on 2018/07/06 at 14:43:03

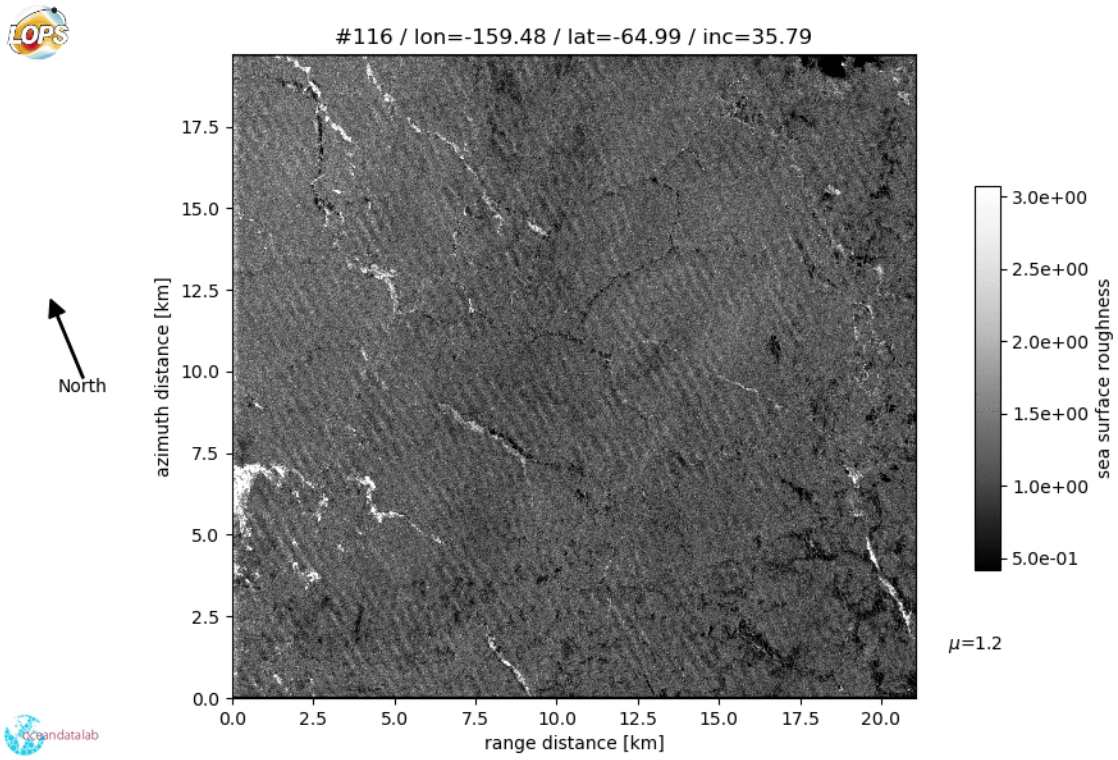


Figure S14: acquired by Sentinel 1B on 2018/07/06 at 14:44:18

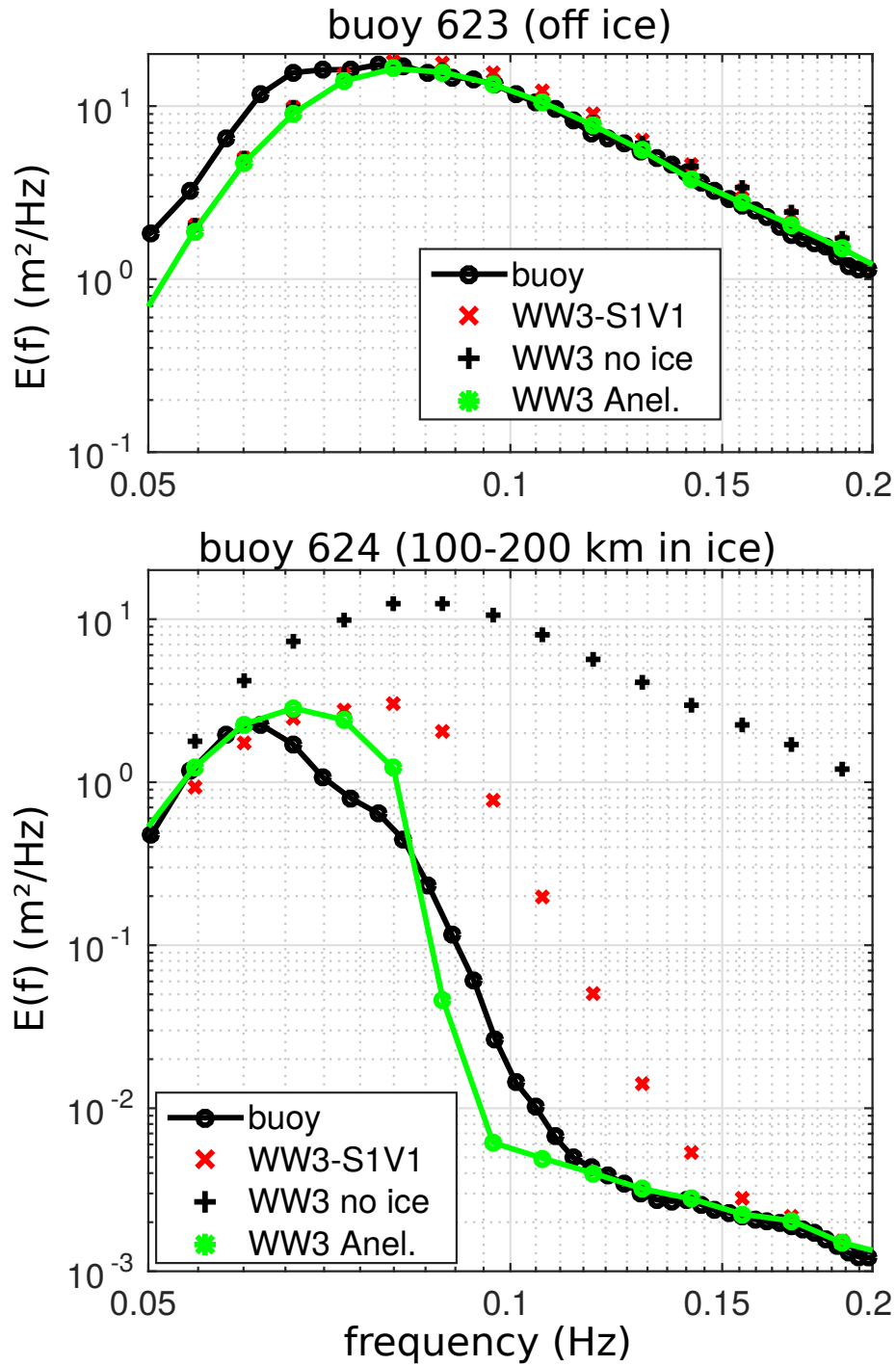


Figure S16: Mean spectra at buoys 623 and 624, from June 12 to July 12.